ADVANCED OPTICAL MATERIALS
www.advopticalmat.de

Sensitivity Enhancement in Photoconductive Light Field Sampling

Najd Altwaijry, Muhammad Qasim, Dmitry Zimin, Nicholas Karpowicz, and Matthias F. Kling**

The emerging field of lightwave electronics is driving optoelectronic information processing beyond current classical limitations and has the potential to eventually reach petahertz frequencies. One of the major obstacles in reaching not only higher switching frequencies but also higher repetition rates with low-power light sources is the efficiency of related devices. A device is presented based on a multilayered material that shows a 13-fold enhancement in terms of converting light to electric current compared to bulk solids. Furthermore, the device exhibits an almost flat intensity response within its working range. The outstanding properties of engineered multilayered devices promise to push technology for lightwave electronics applications.

1. Introduction

Ultrafast optoelectronics is a rapidly growing field of science, uniting the fundamental fields of optics and electronics to create cutting-edge devices capable of efficient and rapid switching of charge carriers, triggered by the incident electric field of strong few-cycle laser pulses.[1] For instance, on one hand, measuring a current flow can be utilized to unambiguously characterise an incident test electric field up to PHz frequencies,[2–5] providing access to the temporal evolution of the electric field of optical pulses. This foundational concept of field-resolved metrology paves the way for extensive and precise investigations of electronic processes in diverse media. It provides sub-cycle resolution of coherent energy transfer dynamics in solids,[6,7] precise time-resolved measurements of the photoelectric effect,[8–10] and real-time investigations of ultrafast many-body dynamics.[11–16] On the other hand, a tailored incident electric field can be used to control the current flow within an optoelectronic device in a transistor-like fashion, leading to PHz optical gates.[17,18] This concept naturally followed the notable progress of optical-field induced currents in dielectrics, which laid the foundation for ultrafast optoelectronic switching.[19–21] In both instances, speed and sensitivity are two crucial parameters of ultrafast optoelectronic devices. The larger the frequency bandwidth of the device, the faster the light-matter information exchange; the higher the sensitivity, the lower the light intensities needed. The speed of operation is typically limited by the response time of the medium, while the sensitivity is limited by the light-matter interaction cross-section. Maximizing the light-matter information exchange is therefore dependent on these two parameters and the optimization thereof.

Various physical constraints limit the performance and efficiency of traditional electronic switches, an example of which is electron mobility which typically decreases as a function of the material bandgap,[22] affecting the lower threshold of switching capabilities, as materials with larger bandgaps exhibit the potential for faster switching. This limitation led to the development of high-electron-mobility transistors, which have outperformed their silicon-based counterparts, achieving a remarkable cutoff switching frequency of 1.5 THz. This breakthrough development paved the way for the realization of the first solid-state amplifier operating beyond the 1 THz threshold.[23] In the case of solid optoelectronic devices, similar restrictions on pulse energy, band structure and bandwidth exist. Relying on strong-field, few-cycle laser pulses increases the chances of charge transfer to higher conduction bands, limiting the fidelity of optoelectronic control.[18] These constraints drive the development of new technologies requiring low pulse energies, e.g., frameworks that exploit field enhancement in nanostructures[3] or devices analogous to the Auston switch.[18,24]

N. Altwaijry, M. Qasim, D. Zimin, N. Karpowicz, M. F. Kling
Max Planck Institute of Quantum Optics
85748 Garching, Germany
E-mail: nicholas.karpowicz@mpq.mpg.de; kling@stanford.edu
N. Altwaijry, M. Qasim, D. Zimin, N. Karpowicz, M. F. Kling
Department of Physics
Ludwig-Maximilians-Universität
85748 Garching, Germany
M. F. Kling
SLAC National Accelerator Laboratory
Menlo Park, CA 94025, USA
M. F. Kling
Applied Physics Department
Stanford University
Stanford, CA 94305, USA

The ORCID identification number(s) for the author(s) of this article can be found under https://doi.org/10.1002/adom.202302490

DOI: 10.1002/adom.202302490

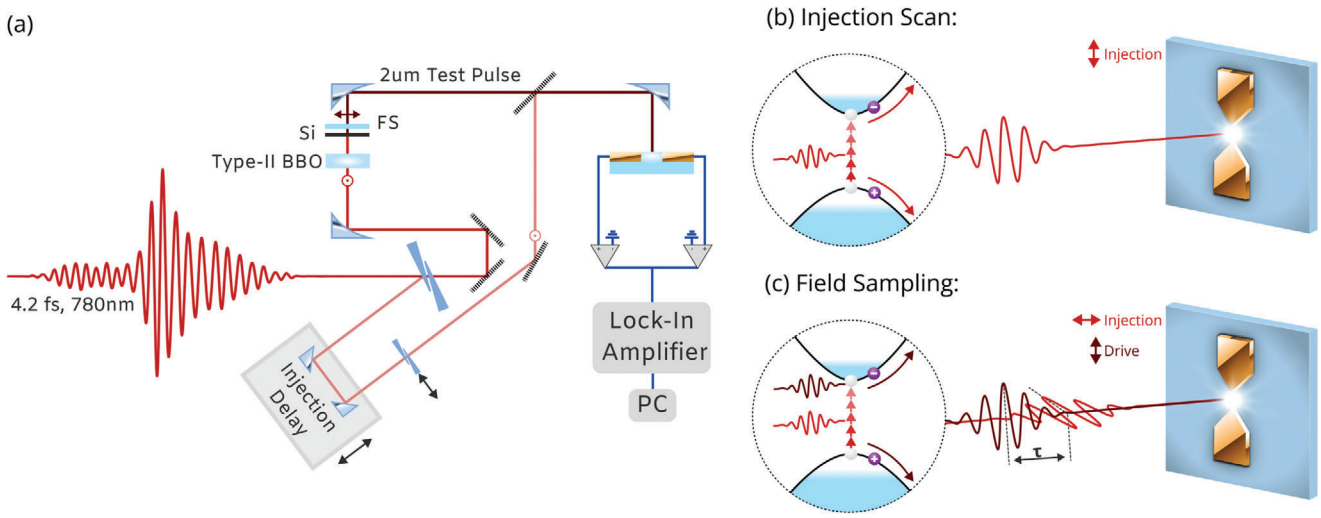

Figure 1. a) NPS measurement setup. A 4.2 fs, 1.86 W white-light pulse (WL) (dark red), centred around 780 nm, is split into two arms, one to generate the test pulse (brown) and one for injection (light red), forming a Mach-Zender-type interferometer. The 3 mW injection arm is formed by taking a reflection from the fused silica wedge pair used for fine-tuning the dispersion of the WL pulse. The remainder of the power is used to generate the 30 µW, 2.1 µm test pulse in a 500 µm thick, Type-II BBO using intra-pulse difference frequency generation. A silicon wafer (Si) is used after the BBO crystal to eliminate the residual WL, permitting the orthogonally polarised 2.1 µm light to pass through to a thin 1 mm fused silica (FS) substrate, which is used for compressing the 2.1 µm output. Several wire-grid polarisers are used to control the power in each arm and a final wire-grid polariser is used to combine the two orthogonal pulses for NPS. b) Injection scan. Here, a single pulse is employed to both inject and drive the carriers in the medium. Note that the polarization of the pulse is parallel to the electrodes. c) Field measurement. Here, a two pulse scheme is implemented. The injection pulse, oriented perpendicular to the electrodes, injects carriers and the drive pulse, oriented parallel to the electrodes, drives the carriers in their respective bands.

Although the aforementioned devices provide PHz-scale switching speeds regardless of the interaction medium, they all possess poor efficiency due to the higher threshold for carrier generation and the limited mobility of the charge carriers. Here, we demonstrate that the device efficiency can be increased by tailoring the medium properties using a nanoscale multilayer coating, comprised of ten alternating layers of 100 nm thick fused silica and silicon, henceforth referred to as layered material (LM). We compare nonlinear photoconductive sampling (NPS) measurements using the LM to bulk silica and find, on average, a 13-fold higher generated current in the LM. Moreover, we implemented our device to measure the electric field of a test pulse and find that the sampled test field is largely independent of the field strength of the driving pulse for the LM, and lower field strengths are required for reaching a stable sampling regime. Our results demonstrate a simple and accessible approach for enhancing the response of optoelectronic devices for field sampling and field-resolved spectroscopy that can reach PHz frequencies.

2. Results and Discussion

Nonlinear photoconductive sampling is a technique that measures the electric field of a test pulse based on the interaction of two pulses in gaseous[25,26] or solid[2] media. In the case of solids, a strong-field ionising pulse, denoted as the injection pulse, interacts with a large bandgap material, leading to an abrupt modification of the material's charge distribution by generating free charge carriers. The induced charge carriers (electrons and holes) constitute a transient gating event and can be subsequently driven in their respective bands by a waveform-stable test field, forming a macroscopic dipole in the medium. Electrodes contacted to the sample detect and screen the induced dipole, generating a potential difference between the electrodes and the ground of an external circuit. This potential difference provides an electromotive force capable of driving a photocurrent proportional to the vector potential of the test field following the expression:

$$J(\tau) = \int_{-\infty}^{\infty} dt\, \vec{A}_{\text{test}}(t) G_{\text{inj}}(t-\tau) \tag{1}$$

where $A_{\text{test}}(t)$ is the vector potential of the test field and $G_{\text{inj}}(t-\tau)$ is the gating function, proportional to the rate of energy deposition in the medium. Note that the mean free path of charge carriers in solid media is typically on the order of a few tens of nanometers[27] and that the electrode separation of an NPS device is typically on the order of a few hundred microns. Therefore, the obtained signal originates from the net displacement of charge carriers through the external circuit, not from carriers directly reaching the electrodes.[28] To demonstrate the aforementioned enhancement in the efficiency of the device, we performed a single-pulse experiment to evaluate the signal generated by fused silica and the LM, as shown in the experimental setup in **Figure 1a**. For a single-pulse measurement, illustrated in Figure 1b, the test arm (brown) was blocked entirely. The injection arm was oriented with the polarization of the light aligned parallel to the electrodes. In this scenario, the pulse both injects and drives the carriers in the medium. A pair of motorized wedges in the beam path serve to modify the dispersion of the pulse. The measured lock-in signal shown in **Figure 2** displays an oscillatory behavior with respect to the wedge insertion Δx and is periodic with a carrier-envelope phase (CEP) change

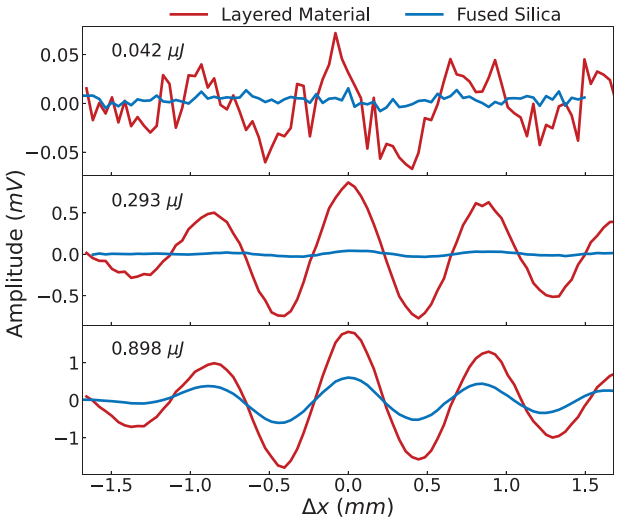

Figure 2. Current amplitude as a function of wedge position Δx. The injection power is increased while maintaining the same focal spot size of 45 μm. The results shown are an average of five measurements.

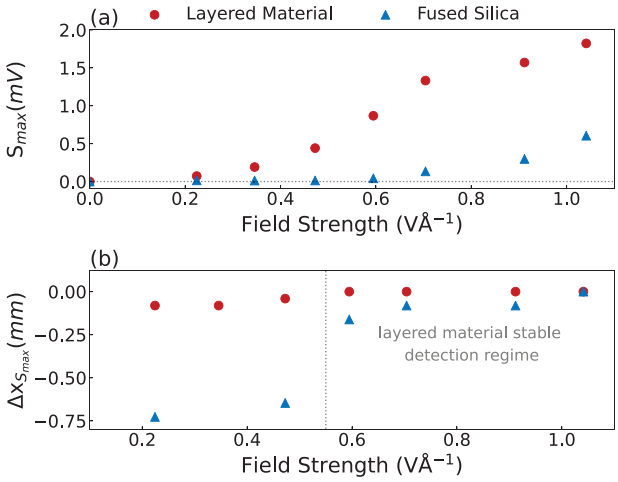

Figure 3. Injection scan determining stable operation. a) Comparison between the maximum signal as a function of field strength at $\Delta x = 0$ for the LM (circles) and fused silica (triangles). b) Relative shift of the zero-crossing of the signal as a function of field strength.

of 2π in agreement with.[2,19,20,29] The envelope of the oscillation exhibits a decrease in the magnitude of the signal, which can be attributed to a decrease in the applied laser field strength due to pulse broadening. When compared to fused silica, it is evident that the LM yields a significant enhancement in the magnitude of the generated signal. The signal exhibits sufficient strength to be effectively recorded using a standard oscilloscope. Since the experiments were conducted consecutively and using the same pulse in both materials, the difference in the magnitude of the generated signal originates from the difference in the number of photoinjected carriers. As seen in Figure 2, with injection energies as low as 42 nJ, it is possible to detect a CEP-dependent current with the LM device.

Using eight different power settings, the maximum photoinjected signal S_{max} at wedge position $\Delta x = 0$ is plotted as a function of field strength in **Figure** 3a for both the LM and fused silica, demonstrating a significant increase in the induced charge carriers using the LM. For instance, as shown in Figure 3a, for a field strength of 0.47 VÅ^{-1}, the LM yields a 31 times higher signal than fused silica (on average yielding a 13-fold increase). Similar to Ref. [29], a relative shift in the zero-crossing of the signal with respect to the wedge position is observed for both the LM and fused silica as a function of field strength, illustrated in Figure 3b. For an optoelectronic device capable of providing reliable field and thus phase information, it is important that the measured phase of the test field is decoupled from that of the injection field strength. We identify a stable regime where this is the case in Figure 3b, such that the zero-crossing of the signal with respect to the wedge position no longer varies with the field strength of the injection pulse. This definition limits the coupling of intensity noise into perceived phase noise, previously thought of as an intrinsic property of media.[29] Moreover, among the reasons that contribute to the heightened performance of the LM is that the higher generated current permits us to arrive at the desired stable detection regime earlier than fused silica[29] or gallium nitride,[20] as indicated by the dotted line in Figure 3b.

As a proof-of-principle, we performed a two-pulse NPS measurements using the LM and fused silica, shown in Figure 1c. For this measurement, we selected a field strength of 0.70 VÅ^{-1} for the injection pulse, in reference to the initial manifestation of a measurable current using fused silica shown in Figure 3a. The test pulse is a 30 μW, 2.1 μm pulse (brown) shown in Figure 1a. **Figure** 4a plots the 2.1 μm test waveform as recorded via NPS using the LM and fused silica, while Figure 4b illustrates the

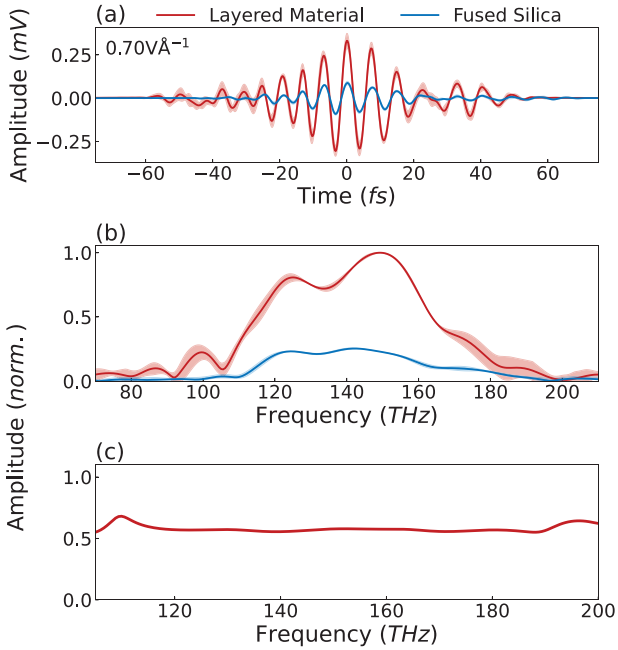

Figure 4. a) Waveform comparison between the LM and fused silica for a field strength of 0.7 VÅ^{-1} as measured via lock-in. b) Spectrum of the measured waveform. The shading represents the standard deviation of five measurements. c) LM response, demonstrating an overall uniform response over the working range of the device.

spectra acquired through Fast Fourier Transform analysis. Note that the LM exhibits significantly higher sensitivity compared to fused silica, with considerable overlap in terms of waveform shape and frequency content. Figure 4c illustrates the response of the LM. As can be seen, the LM yields an overall uniform response across the designated region of detection interest.

3. Theoretical Analysis

To understand the intricate details of the light-matter interaction, we theoretically modeled the evolution of the electric field and induced polarization from generated charge carriers in fused silica and the LM. The model solves the differential equation:

$$\left(\frac{\partial^2}{\partial z^2} - \frac{1}{c^2}\frac{\partial^2}{\partial t^2}\right)\vec{E}(z,t) = \mu_0 \frac{\partial^2}{\partial t^2}\vec{P}(z,t) \tag{2}$$

where $\vec{E}(z,t)$ is the electric field, $\vec{P}(z,t)$ is the polarization and z is the propagation direction, on a 1D grid and calculates the charge density created by the injection field based on multiphoton ionization. The Runge-Kutta-4 numerical method of solving differential equations is employed[30] to numerically approximate the solution to the differential equation, providing information on the field, the polarization, and the charge density in the medium. The charge density $J(t)$ is then evaluated using the Drude model,[31,32] such that $J(t) = ne^2\tau\vec{E}(t)/m$. To this end, we propagated a 9 fs linearly polarized super-gaussian pulse of order 4, centred around 400 THz through the medium.

Figure 5a illustrates the evolution of the charge density across a 1 µm thick fused silica sample. In the initial stage of interaction, at $t = 0$ fs, the charge carriers build inside the medium as a consequence of Equation (2). We further plot the dynamic evolution of the charge carriers at $t = 0.5$ fs and $t = 10$ fs. It is evident from the plot that the evolution of charge carriers in the medium is contingent on the propagation of the pulse in the sample before finally accumulating on the exit surface, defining a skin depth of a few hundred nanometers at $t = \infty$, in agreement with studies examining the strong field optical breakdown threshold[33] and the ultrafast time-resolved evolution of laser-excited carrier densities in fused silica.[34] We refer to this current at $t = \infty$ as the cumulative charge density $J_{cumulative}$, as it plays a role in gating the test field in an NPS measurement. Note that for fused silica, the pulse experiences a group velocity dispersion of 40.44 fs^2 per mm, which remains a negligible quantity for a sample thickness of 1 µm. Considering the geometry of the sample as depicted in Figure 1b,c, with the electrodes affixed on top of the surface of the sample, and recognising that the electric field behavior of a dipole moment diminishes with $1/r^3$, we conclude that the predominant contribution of charge carriers originates close to the surface of the sample, in accordance with previous experiments using step-like electrodes, which have shown that the cumulative charge density is maximum after a depth of 20 µm, beyond which the injection pulse disperses and the CEP changes by $\pi/2$.[35] Similar to fused silica, an identical calculation was performed for the LM, comprised of ten alternating 100 nm thick layers of fused silica and silicon as shown in Figure 5b, where we plot the cumulative current only. From our simulations, it appears that the charge accumulates at the interface between the two materials, concurrent with.[36] Figure 5c compares the cumulative charge density contributing to the transient gate function in silicon and in fused silica. As illustrated, the cumulative charge density is mostly provided by silicon, with $J(t_\infty)$ for silicon orders of magnitude larger than $J(t_\infty)$ for fused silica. We attribute this difference in the probability amplitude of the photo-ionisation process, given by Fermi's golden rule (ionization cross-section). This observation indicates that the injection pulse is predominantly absorbed within the silicon layer, inducing the generation of electron-hole pairs. Subsequently, these electron-hole pairs diffuse toward the interface between silicon and fused silica,[36] where they are driven by the applied test field, forming a detectable macroscopic dipole in the sample. As shown, the theoretical calculations support the experimentally observed increase in sensitivity of the LM device.

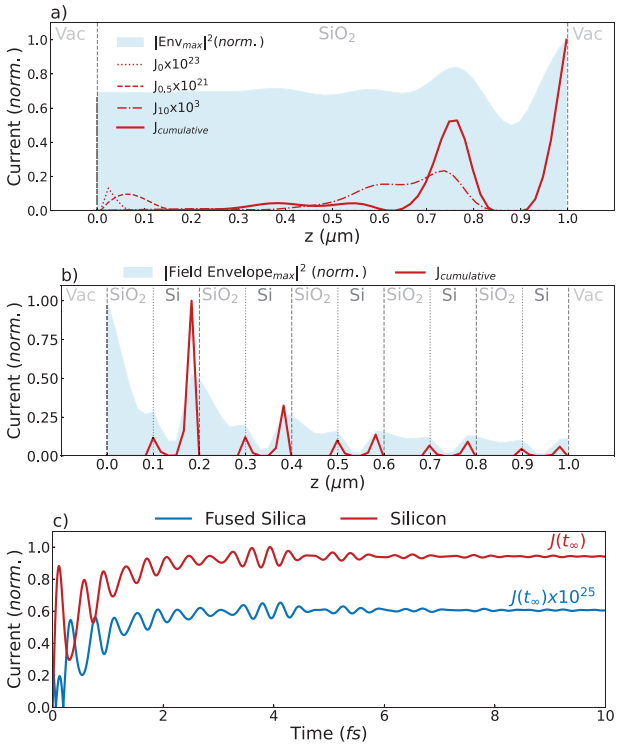

Figure 5. a) Calculated charge density generated inside a 1 µm thick fused silica (SiO_2) sample. The shaded area (blue) depicts the intensity maximum of the injection field. At an elapsed time of $t = 0$ fs (red dotted), the charge begins accumulating in the medium. The charge accumulation increases for $t = 0.5$ fs (red dashed), and continues increasing as a function of time as shown for $t = 10$ fs (red dashed-dotted). Once the injection pulse leaves the medium and the ringing due to internal reflections has subsided, the cumulative charge density is plotted in red (solid line). b) Calculated cumulative charge density (red) generated using a LM comprised of alternating layers of fused silica and silicon. The shaded area (blue) represents the intensity maximum of the injection field. c) Comparison between the cumulative charge density generated in fused silica versus the cumulative charge density generated in silicon for the LM in (b), indicating that the majority of the charge density is generated in the silicon layer.

4. Conclusion

We have demonstrated an optoelectronic device, based on a layered material instead of a bulk solid, with an enhanced response for ultrafast field sampling. Due to the 13-fold increase in signal compared to a bulk solid device, it has the potential of passively measuring laser fields in laser systems with low pulse energy, such as oscillators, offering a step forward in field-resolved spectroscopy in low-energy systems. More importantly, we find that the sampled test field is largely insensitive to the driving field intensity over the operating range of the device. The straightforward and easily realizable configuration of our engineered sample paves the way toward exploiting such devices in practical applications. Among these are not only measurements of laser fields for characterizing ultrashort light pulses but also their application in spectroscopy, where small changes in the transmitted or reflected waveform from a sample of interest can be captured.

5. Experimental Section

Sample Preparation: The layered sample employed in this manuscript was fabricated in-house by alternately sputtering silicon and fused silica onto a thin fused silica substrate (Valley Design corp.) in the following order: Substrate ⇒ SiO_2 ⇒ Si... ⇒ SiO_2. The layers were applied at the coating facility at the Ludwig-Maximillian-Universität München. The electrodes were subsequently deposited at the Center for Nanotechnologies and Nanomaterials at the Walter Schottky Institute, using a custom laser-cut shadow mask, by coating a thin layer (5 nm) of chromium, followed by a thick layer of gold (150 nm). Both stages were performed through physical vapor deposition using electron beams. The electrode deposition, soldering and wiring procedures for the sample were performed by the author. Rigorous testing of the samples was performed to ensure the absence of short circuits or any significant resistance.

Data Analysis: The current amplitude shown in Figure 2 represents an average of five measurements (raw data). The waveforms in Figure 4a are processed by applying a supergaussian bandpass filter of the form: $SG(\nu) = \exp\left[-\frac{\nu-\nu_0}{2\sigma}\right]^{10}$, where $\nu_0 = 145$ THz and $\sigma = 100$ THz.

Acknowledgements

The authors are grateful to Vladislav Yakovlev for fruitful discussions and to Ferenc Krausz for providing the experimental infrastructure at MPQ. The authors thank Florian Pantle for his assistance during the preparation of the electrodes. This work is supported by the European Union under grant EU-H2020 654148 (Laserlab Europe) and the FETopen project PetaCOM. The authors acknowledged support by the Air Force Office of Scientific Research under grant FA9550-16-1-0073. M.F.K.'s work at SLAC is supported by the U.S. Department of Energy, Office of Science, Basic Energy Sciences, under DE-AC02-76SF00515 and the Chemical Sciences, Geosciences, and Biosciences Division (CSGB). N.A. was part of the Max Planck School of Photonics supported by BMBF, Max Planck Society, and Fraunhofer Society. N.A., M.Q., and D.Z. acknowledged support by the Max Planck Society via the IMPRS for Advanced Photon Science.

Open access funding enabled and organized by Projekt DEAL.

Conflict of Interest

The authors declare no conflict of interest.

Data Availability Statement

The data that support the findings of this study are available from the corresponding author upon reasonable request.

Keywords

field sampling metrology, heterostructure, ultrafast optics

Received: October 3, 2023
Revised: February 4, 2024
Published online: March 6, 2024

[1] D. Hui, H. Alqattan, S. Zhang, V. Pervak, E. Chowdhury, M. T. Hassan, *Sci. Adv.* **2023**, *9*, eadf1015.
[2] S. Sederberg, D. Zimin, S. Keiber, F. Siegrist, M. S. Wismer, V. S. Yakovlev, I. Floss, C. Lemell, J. Burgdörfer, M. Schultze, F. Krausz, N. Karpowicz, *Nat. Commun.* **2020**, *11*, 430.
[3] M. R. Bionta, F. Ritzkowsky, M. Turchetti, Y. Yang, D. Cattozzo Mor, W. P. Putnam, F. X. Kärtner, K. K. Berggren, P. D. Keathley, *Nat. Photonics* **2021**, *15*, 456.
[4] E. Ridente, M. Mamaikin, N. Altwaijry, D. Zimin, M. F. Kling, V. Pervak, M. Weidman, F. Krausz, N. Karpowicz, *Nat. Commun.* **2022**, *13*, 1111.
[5] A. Herbst, K. Scheffter, M. M. Bidhendi, M. Kieker, A. Srivastava, H. Fattahi, *J. Phys. B: At., Mol. Opt. Phys.* **2022**, *55*, 172001.
[6] M. Schultze, E. M. Bothschafter, A. Sommer, S. Holzner, W. Schweinberger, M. Fiess, M. Hofstetter, R. Kienberger, V. Apalkov, V. S. Yakovlev, M. I. Stockman, F. Krausz, *Nature* **2013**, *493*, 75.
[7] A. Sommer, E. M. Bothschafter, S. A. Sato, C. Jakubeit, T. Latka, O. Razskazovskaya, H. Fattahi, M. Jobst, W. Schweinberger, V. Shirvanyan, V. S. Yakovlev, R. Kienberger, K. Yabana, N. Karpowicz, M. Schultze, F. Krausz, *Nature* **2016**, *534*, 86.
[8] R. Pazourek, S. Nagele, J. Burgdörfer, *Rev. Mod. Phys.* **2015**, *87*, 765.
[9] F. Siek, S. Neb, P. Bartz, M. Hensen, C. Strüber, S. Fiechter, M. Torrent-Sucarrat, V. M. Silkin, E. E. Krasovskii, N. M. Kabachnik, S. Fritzsche, R. D. Muiño, P. M. Echenique, A. K. Kazansky, N. Müller, W. Pfeiffer, U. Heinzmann, *Science* **2017**, *357*, 1274.
[10] M. Ossiander, J. Riemensberger, S. Neppl, M. Mittermair, M. Schäffer, A. Duensing, M. S. Wagner, R. Heider, M. Wurzer, M. Gerl, M. Schnitzenbaumer, J. V. Barth, F. Libisch, C. Lemell, J. Burgdörfer, P. Feulner, R. Kienberger, *Nature* **2018**, *561*, 374.
[11] M. Kira, S. Koch, *Prog. Quantum Electron.* **2006**, *30*, 155.
[12] A. L. Cavalieri, N. Müller, T. Uphues, V. S. Yakovlev, A. Baltuška, B. Horvath, B. Schmidt, L. Blümel, R. Holzwarth, S. Hendel, M. Drescher, U. Kleineberg, P. M. Echenique, R. Kienberger, F. Krausz, U. Heinzmann, *Nature* **2007**, *449*, 1029.
[13] M. Ossiander, F. Siegrist, V. Shirvanyan, R. Pazourek, A. Sommer, T. Latka, A. Guggenmos, S. Nagele, J. Feist, J. Burgdörfer, R. Kienberger, M. Schultze, *Nat. Phys.* **2017**, *13*, 280.
[14] J. Riemensberger, S. Neppl, D. Potamianos, M. Schäffer, M. Schnitzenbaumer, M. Ossiander, C. Schröder, A. Guggenmos, U. Kleineberg, D. Menzel, F. Allegretti, J. V. Barth, R. Kienberger, P. Feulner, A. G. Borisov, P. M. Echenique, A. K. Kazansky, *Phys. Rev. Lett.* **2019**, *123*, 176801.
[15] J. Freudenstein, M. Borsch, M. Meierhofer, D. Afanasiev, C. P. Schmid, F. Sandner, M. Liebich, A. Girnghuber, M. Knorr, M. Kira, R. Huber, *Nature* **2022**, *610*, 290.
[16] D. A. Zimin, N. Karpowicz, M. Qasim, M. Weidman, F. Krausz, V. S. Yakovlev, *Nature* **2023**, *618*, 276.
[17] T. Boolakee, C. Heide, A. Garzón-Ramírez, H. B. Weber, I. Franco, P. Hommelhoff, *Nature* **2022**, *605*, 251.
[18] M. Ossiander, K. Golyari, K. Scharl, L. Lehnert, F. Siegrist, J. P. Bürger, D. Zimin, J. A. Gessner, M. Weidman, I. Floss, V. Smejkal, S. Donsa, C. Lemell, F. Libisch, N. Karpowicz, J. Burgdörfer, F. Krausz, M. Schultze, *Nat. Com.* **2022**, *13*, 1620.

[19] A. Schiffrin, T. Paasch-Colberg, N. Karpowicz, V. Apalkov, D. Gerster, S. Mühlbrandt, M. Korbman, J. Reichert, M. Schultze, S. Holzner, J. V. Barth, R. Kienberger, R. Ernstorfer, V. S. Yakovlev, M. I. Stockman, F. Krausz, *Nature* **2013**, *493*, 70.
[20] T. Paasch-Colberg, S. Y. Kruchinin, Özge Sağlam, S. Kapser, S. Cabrini, S. Muehlbrandt, J. Reichert, J. V. Barth, R. Ernstorfer, R. Kienberger, V. S. Yakovlev, N. Karpowicz, A. Schiffrin, *Optica* **2016**, *3*, 1358.
[21] T. Higuchi, C. Heide, K. Ullmann, H. B. Weber, P. Hommelhoff, *Nature* **2017**, *550*, 224.
[22] D. L. Rode, *Phys. Rev. B* **1970**, *2*, 1012.
[23] X. Mei, W. Yoshida, M. Lange, J. Lee, J. Zhou, P.-H. Liu, K. Leong, A. Zamora, J. Padilla, S. Sarkozy, R. Lai, W. R. Deal, *IEEE Electron Device Lett.* **2015**, *36*, 327.
[24] N. Altwaijry, M. Qasim, M. Mamaikin, J. Schötz, K. Golyari, M. Heynck, E. Ridente, V. S. Yakovlev, N. Karpowicz, M. F. Kling, *Adv. Opt. Mater.* **2023**, *11*, 2202994.
[25] A. Korobenko, K. Johnston, M. Kubullek, L. Arissian, Z. Dube, T. Wang, M. Kübel, A. Y. Naumov, D. M. Villeneuve, M. F. Kling, P. B. Corkum, A. Staudte, B. Bergues, *Optica* **2020**, *7*, 1372.
[26] D. Zimin, M. Weidman, J. Schötz, M. F. Kling, V. S. Yakovlev, F. Krausz, N. Karpowicz, *Optica* **2021**, *8*, 586.
[27] R. Jung, J. Lee, G. Orosz, A. Sulyok, G. Zsolt, M. Menyhard, *Surf. Sci.* **2003**, *543*, 153.
[28] J. Schötz, A. Maliakkal, J. Blöchl, D. Zimin, Z. Wang, P. Rosenberger, M. Alharbi, A. M. Azzeer, M. Weidman, V. S. Yakovlev, B. Bergues, M. F. Kling, *Nat. Commun.* **2022**, *13*, 962.
[29] T. Paasch-Colberg, A. Schiffrin, N. Karpowicz, S. Kruchinin, Ö. Sağlam, S. Keiber, O. Razskazovskaya, S. Mühlbrandt, A. Alnaser, M. Kübel, V. Apalkov, D. Gerster, J. Reichert, T. Wittmann, J. V. Barth, M. I. Stockman, R. Ernstorfer, V. S. Yakovlev, R. Kienberger, F. Krausz, *Nat. Photonics* **2014**, *8*, 214.
[30] J. Butcher, *Appl. Numer. Math.* **1996**, *20*, 247.
[31] P. Drude, *Ann. Phys.* **1900**, *306*, 566.
[32] P. Drude, *Ann. Phys.* **1900**, *308*, 369.
[33] M. Lenzner, J. Krüger, S. Sartania, Z. Cheng, C. Spielmann, G. Mourou, W. Kautek, F. Krausz, *Phys. Rev. Lett.* **1998**, *80*, 4076.
[34] F. Quéré, S. Guizard, P. Martin, *Europhys. Lett.* **2001**, *56*, 138.
[35] S. Keiber, Ph.D. thesis, Ludwig-Maximilians-Universität München, Geschwister-Scholl-Platz 1, 80539 München, **2016**.
[36] S. R. Ellis, N. C. Bartelt, F. Léonard, K. C. Celio, E. J. Fuller, D. R. Hughart, D. Garland, M. J. Marinella, J. R. Michael, D. W. Chandler, B. Liao, A. A. Talin, *Phys. Rev. B* **2021**, *104*, L161303.